ROYAL SOCIETY OF CHEMISTRY

Check for updates

Hückel anion based concentrated electrolytes for lithium–sulfur batteries

Aginmariya Kottarathil, [ID] *[abc] N. Tan Luong, [ID] [b] Carolina Cruz Cardona, [ID] [b] Steffen Jeschke,[d] Tomooki Hosaka, [ID] [b] Grażyna Zofia Żukowska,[a] Maciej Marczewski,[a] Władysław Wieczorek[ac] and Patrik Johansson [ID] *[bc]

Hückel anion-based lithium salts present a promising alternative to conventional LiTFSI electrolytes for lithium–sulfur (Li–S) batteries by reducing lithium polysulfide (LiPS) solubility while maintaining favourable electrochemical properties. This study systematically investigates the performance of LiTDI, LiPDI, and LiHDI-based electrolytes in a DOL : DME (1 : 1) solvent system. Raman spectroscopy, ionic conductivity, and viscosity measurements reveal distinct ion association behaviours, with molecular dynamics simulations confirming preferential Li$^+$ solvation by DME. Electrochemical cycling tests demonstrate stable discharge capacities, particularly at higher salt concentrations. *Operando* Raman spectroscopy provides direct insight into LiPS evolution, confirming that higher salt concentrations slow down LiPS dissolution and diffusion, mitigating the LiPS shuttle effect. Additionally, COSMO-RS modeling predicts significantly reduced Li$_2$S$_8$ solubility with increasing salt concentration. These findings highlight the potential of Hückel anion-based electrolytes in advancing high-performance Li–S battery technologies.

1 Introduction

The development of high-performance, sustainable, and cost-effective batteries is crucial to meet the growing demand for next-generation energy storage systems. Among various approaches, optimizing electrolytes plays a fundamental role in improving battery performance and longevity. Electrolytes serve as the medium for the migration of cations between the positive and negative electrodes, and their design, development, and optimization are essential for enhancing battery efficiency.[1,2]

New electrolyte formulations for lithium-ion and next generation batteries (NGBs) include the use of new types of lithium salts such as those based on Hückel anions. These are aromatic molecules characterized by delocalized π-electrons following Hückel's rule (4n + 2), of which n is any non-negative integer.[3] These anions exhibit unique π–π interactions, primarily driven by dispersion forces and weak electrostatic interactions with counterions. The nitrogen atoms in the aromatic ring interact only weakly with lithium cations, leading to unique solvation and ion mobility properties.[4,5] Given their influence on ion solvation and conductivity, Hückel anion-based lithium salts

are particularly attractive for lithium ion batteries (LIBs) and NGBs, including lithium–sulfur (Li–S) batteries.[5]

Li–S batteries have emerged as promising NGB candidates due to their high theoretical capacity, low cost, and environmental friendliness.[6–8] However, significant challenges include poor cell performance resulting from low initial sulfur utilization and rapid capacity fading, mainly due to the dissolution and shuttling of lithium polysulfides (Li(PS)) (long-chain Li$_2$S$_x$, $4 < x < 8$) during battery cycling.[9,10] Limiting LiPS solubility is crucial for suppressing the LiPS shuttle mechanism. This also helps to protect the lithium metal anode, ultimately enhancing the cycling performance.[11] Recent research has focused on designing electrolytes with reduced LiPS solubility by exploring alternative lithium salts or increasing the lithium salt concentration.[12–14]

Currently, the most common Li–S battery electrolytes are based on lithium bis(trifluoromethanesulfonyl)imide (LiTFSI) dissolved in 1,2-dimethoxyethane and 1,3-dioxolane (DOL : DME, 1 : 1 v/v).[15,16] LiTFSI is widely used due to its high ionic conductivity, chemical stability, and compatibility with ether solvents.[15] However, there is growing interest in alternative electrolyte formulations with lower LiPS solubility.[13]

Reducing the solubility of LiPSs and minimizing their interactions with the electrolyte are key strategies to suppress the shuttling effect in Li–S cells. Recently, electrolytes based on lithium salts of Hückel anions, in particular lithium 4,5-dicyano-2-(trifluoromethyl)imidazole (LiTDI), have emerged as promising candidates.[5,17] As compared to conventional LiTFSI-based electrolytes, they exhibit lower ionic conductivity,[18] but

[a] *Warsaw University of Technology, Faculty of Chemistry, 00664, Warszawa, Poland. E-mail: aginmariya.kottarathil@pw.edu.pl*

[b] *Chalmers University of Technology, Department of Physics, 412 96, Gothenburg, Sweden. E-mail: patrik.johansson@chalmers.se*

[c] *Alistore-ERI, CNRS FR 3104, 15 Rue Baudelocque, 80039 Amiens, France*

[d] *Centre for Catalysis and Clean Energy, School of Environment and Science, Griffith University, Gold Coast campus, QLD 4215, Australia*
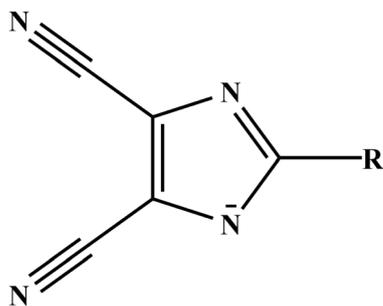
Fig. 1 Chemical structures of the Hückel anions (TDI, PDI and HDI) used in this work; $R_1 = CF_3$, $R_2 = C_2F_5$, $R_3 = C_3F_7$.

LiTDI-based electrolytes result in an 83% lower Li_2S_8 solubility under identical conditions.[11] This is attributed to differences in lithium solvation, resulting in formation of Li_2S_4 dimers.[11] The TDI anion was reported to have lower mobility compared to various other anions including TFSI, which combined with its less preferential interaction with LiPSs, contributes to relatively better Li–S battery performance.[13]

Although LiTDI has demonstrated significant improvements in Li–S battery performance,[11,18] its higher derivatives, lithium 4,5-dicyano-2-(pentafluoroethyl)imidazole (LiPDI) and lithium 4,5-dicyano-2-(heptafluoropropyl)imidazole (LiHDI) (Fig. 1)—which differ solely in the length of their perfluorinated alkyl chains—have yet to be explored in the context of Li–S batteries. Nonetheless, these salts have been studied across various concentrations in carbonate-based solvent mixtures for LIB electrolytes.[19] Notably, incorporating Hückel anion electrolytes such as LiTDI in LIBs significantly increases lithium-ion transference numbers—nearly doubling them.[20] Additionally, these electrolytes extend LIB lifespan due to their effective H_2O scavenging capability and superior electrochemical stability compared to conventional $LiPF_6$-based systems.[19,20]

Here, we present a comprehensive study of these Hückel anion-based salts in Li–S batteries for the first time. We first explore their local structure in relation to the ion transport properties by Raman spectroscopy and molecular dynamics (MD) simulations. Before we evaluate their electrochemical performance, the solubility of LiPS in these electrolytes is predicted using our previously developed machine learning model based on the conductor-like screening model for real solvents (COSMO-RS).[21] Notably, this work is among the first to leverage *operando* Raman spectroscopy for the direct visualization of LiPS species within these electrolytes.[22–24] Through a combination of experimental techniques and modeling, we aim to elucidate the underlying mechanisms governing the performance of Hückel anion-based electrolytes and provide valuable insights for designing and optimizing electrolyte materials tailored for high-performance Li–S batteries.

2 Experimental and computational methods

Electrolyte preparation

LiTDI, LiPDI and LiHDI were synthesized according to the protocols reported previously,[17] while $LiNO_3$ (99.9%), DOL

(99.8%) and DME (99.8%) were purchased from Sigma-Aldrich. The salts were dried at 140 °C under vacuum overnight before use. All salts and solvents were handled in an argon-filled glove box at all times (<1 ppm H_2O and 2 ppm O_2). The electrolytes were prepared by dissolving (using a magnetic stirrer for 24 h at room temperature) appropriate amounts of salts into a certain amount of the DOL:DME (1 : 1, v/v) solvent mixture to get the desired concentrations, *i.e.*, 0.1, 0.3, 0.6, 1.0 and 2.0 M. For selected electrochemical experiments, 0.2 M $LiNO_3$ was added to the 2.0 M LiHDI electrolyte to evaluate its effect on the Coulombic efficiency (CE) and LiPS shuttling. Our tentative solubility test showed that while LiHDI has higher solubility and could be prepared at 3.0 M, LiTDI and LiPDI became saturated above 2.0 M. Thus, we limit the concentration of all electrolytes to 2.0 M in this study for consistent comparison.

Physicochemical properties of the electrolytes

The densities and viscosities were recorded for 10–50 °C at an interval of 10 °C using an Anton Paar DMA4500M density meter equipped with a Lovis 2000M rolling ball viscometer module. The temperature accuracy was ±0.02 °C and it took approximately 5 min to reach equilibrium. The viscosity values were obtained by averaging the results from at least 5 back-and-forth runs of the rolling ball. Prior to the measurements, the instrument was calibrated and verified using standards.

The ionic conductivities were measured for 0–50 °C at an interval of 10 °C, with a thermal equilibration of at least 30 min, using electrochemical impedance spectroscopy with an A.C. signal of 5 mV in 500 kHz to 10 Hz range with 10 points per decade on a VMP3 instrument from Bio-Logic. Electrolytes were placed into micro conductivity cells with cell constants values = 0.3–0.7 cm^{-1}, which were then put into a cryostat-thermostat system (Haake K75 with the DC50 temperature controller).

Composite cathode preparation

The C/S composite cathode was composed of sulfur, 60 wt%, (Sigma-Aldrich, 99.998% trace metal basis), carbon black (Vulcan) as conductive additive, 38.5%, and sodium carboxymethyl cellulose (Na-CMC, $M_w = 700\,000$, Sigma-Aldrich) as binder, 1.5 wt%. Appropriate quantities of sulfur and carbon black were mixed in mortar to prepare the electrodes. Next, the binder was added, and the solution using water as solvent was mixed magnetically to obtain a homogenous slurry. The electrode suspension was cast on a 20 μm aluminum foil (Hohsen) using the Doctor Blade technique, resulting in a coating with a thickness of 250 μm. After coating, the electrode was dried at 60 °C under vacuum for 24 h. The sulfur loading was approximately 1.36 mg cm^{-2}.

Ex situ Raman spectroscopy

Fourier transform (FT) Raman spectra of the electrolytes were acquired on a Bruker MultiRam spectrometer equipped with a 1064 nm excitation laser and a liquid N_2-cooled Ge detector. The samples were measured at 25 °C in sealed 4-mL glass vials. Each Raman spectrum was obtained by co-adding of 1000 scans at a spectral resolution of 2 cm^{-1}. Spectral data were analyzed as acquired without further normalization step or background

correction. Spectral deconvolution and fitting of the ν_{CN} region (2200–2300 cm^{-1}) were performed with MATLAB (Mathworks, R2023b) using multiple combined Gaussian–Lorentzian (Voigt) components.

The number of coordinated solvent molecules (N) in the primary solvation shell of Li was calculated based on the relationship between (i) the Raman intensities of the peaks corresponding to bound (I_b) and free (I_f) solvent molecules—assuming similar Raman scattering factors—and (ii) the concentrations of the Li salt (c_{Li}) and the solvent ($c_{solvent}$). The relationship is expressed as follows:[25,26]

$$\frac{I_b}{I_f + I_b} = N\frac{c_{Li}}{c_{solvent}} \qquad (1)$$

Operando Raman spectroscopy

The Li–S battery was assembled in an electrochemical cell ECC-Opto-Std (EL-cell® GmbH) in a sandwich configuration similar to a coin cell assembly. The cell included a ⌀10 mm C/S cathode, a ⌀10 mm glass fiber separator (Whatman™ 1821 GF/ B, 675 μm) and a ⌀15 mm Li metal anode with a 2 mm hole at the center. The cell used a borosilicate glass window for observing Raman spectra, and 60 μL of the electrolytes was used. The assembly was performed in an Ar-filled glove box with O$_2$ and H$_2$O levels controlled below 1 ppm.

Operando Raman spectra at 25 °C were collected on a LabRam HR Evolution dispersive Raman spectrometer (Horiba GmbH) in confocal mode using a 633 nm He–Ne laser (3 mW) focused on the sample by a 10× lens, a 200 μm confocal hole, and a Syncerity OE detector. Raman spectra were continuously collected while the cell was cycled at a C/10 rate (1C = 1672 mAh g^{-1}) and voltages between 1–3 V vs. Li$^+$/Li^0 on a GAMRY Series G 300.

Spectral analysis was performed with MATLAB (Mathworks, R2023b) as follows. The strong fluorescence background was first removed before all spectral data were normalized by the standard normal variate method to have zero mean and normal standard deviation. The PS region (300–600 cm^{-1}) was then fitted with combined Gaussian–Lorentzian (Voigt) components to retrieve the contributions of different PS species.

Li–S battery tests

The coin cells (CR2032) were assembled inside the Ar-filled glovebox, with a C/S composite cathode (⌀13 mm), a lithium metal foil anode (⌀14 mm and 200 μm thick), and a Whatman glassfiber (1821 GF/C, 260 μm, 16 mm) separator filled with 70 μL of electrolyte (or 25 μL mg^{-1} S^{-1}). The coin cells were cycled at a C/10 rate (1C = 1672 mAh g^{-1}) and voltages between 1–3 V vs. Li$^+$/Li^0 using a Scribner Associates Incorporated 580 Battery Test System.

Molecular simulations

Classical MD simulations were performed using LAMMPS[27] and the OPLS-AA force field[28] with anion parameters adapted from their neutral counterparts. Partial atomic charges were recalculated using density functional theory (DFT) at the B3LYP/6-31G(d) level with the CHELPG method,[29–31] and a charge scaling factor of 0.8 was applied following established practices for non-polarizable force fields.[32,33]

Simulations were conducted at electrolyte concentrations of 0.3, 0.6, 1.0, and 2.0 M, within a cubic simulation box containing 1500 molecules. The number of anions and solvent molecules varies with concentration (Table S1). The protocol included high-temperature equilibration at 800 K (2 ns) to enhance conformational sampling, cooling to 300 K followed by further equilibration (10 ns), and a 15 ns production run in the NVT ensemble. The Nosé–Hoover thermostat/barostat maintained target conditions, and electrostatic interactions were handled via the PPPM method with periodic boundary conditions.

Radial distribution functions (RDFs) and coordination numbers (CNs) were analyzed using LAMMPS subroutines to assess lithium-ion solvation and ion-pairing trends at different concentrations. Additional methodological details, including force field parameterization and simulation setup, are provided in the SI.

COSMO-RS modeling

The conductor-like screening model for real solvents (COSMO-RS)[34,35] was used to predict the solubility of Li$_2$S$_8$ in the electrolytes.[21] The COSMO-RS calculations were conducted using the COSMOthermX program[36] and the BP-TZVPD-C30-1701 parameterization at a temperature of 293.15 K. The TURBOMOLE V7.1 software package[37] was used to initially optimize the geometries of the molecules/anions using DFT and the BP86 functional and the TZVP basis set in both the gas phase and assuming a perfect conductor[38,39] ($\varepsilon = \infty$). Additionally, single-point calculations were performed using BP86/TZVPD to generate a fine grid cavity. The molecular structures and cosmo-files for LiTDI, LiPDI, LiHDI, TDI, PDI, HDI, DOL and DME were obtained using the TmoleX 4.6.0 graphical user interface and were added to the COSMOthermX database. All COSMO-RS computations were performed for 1.0 and 2.0 M of salt in DOL:DME (1:1, v/v) using mole fractions.[21]

3 Results and discussion

We begin by presenting the physicochemical properties of these electrolytes based on Hückel anions across various salt concentrations, subsequently correlating them with local solvation structures resolved through Raman spectroscopy and MD simulations. Key insights into concentration and anion-driven LiPS solubility in these electrolytes are then explored using predictions from COSMO-RS modeling and visualizations from operando Raman spectroscopy. Finally, these findings are connected to Li–S battery performance.

Ion transport

Several factors influence the ionic conductivity of electrolytes, including anion type, salt concentration, and ionic association dynamics.[40]

In our previous work, we reported that the ionic conductivity of LiTDI in DOL:DME at 20 °C is only slightly lower than that of

18780 | Phys. Chem. Chem. Phys., 2025, **27**, 18778–18788
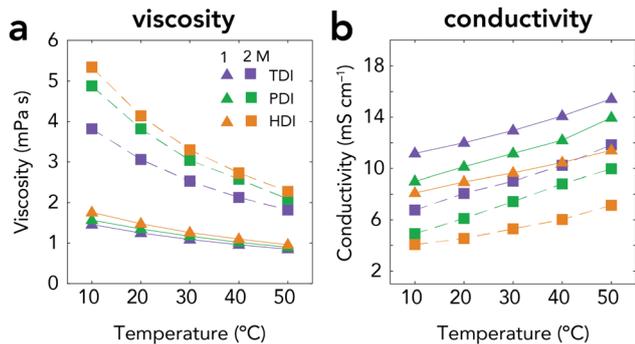
This journal is © the Owner Societies 2025

Fig. 2 Viscosity (a) and ionic conductivity (b) of 1.0 M (solid lines) and 2.0 M (dash lines) LiTDI, LiPDI and LiHDI-based electrolytes.

the commonly used LiTFSI in DOL:DME electrolyte.[18] Here, we compare the viscosities and ionic conductivities of LiTDI, LiPDI, and LiHDI electrolytes. The relationship between ionic conductivity and viscosity as functions of temperature for 1.0 and 2.0 M salt concentrations of LiTDI, LiPDI, and LiHDI in DOL:DME (Fig. 2) shows that as the temperature increases, the ionic conductivity do as well, consistent with the expectation that elevated temperatures reduce viscosity and facilitate ion mobility. As the concentration increases from 1.0 to 2.0 M, ionic conductivity decreases while viscosity increases. The observed trends in ionic conductivity for both concentrations follow the sequence LiTDI > LiPDI > LiHDI, which is inversely related to the viscosity trend. The differences in ionic conductivity are slightly more pronounced at a 2.0 M salt concentration and correlate well with viscosity results.

As compared to LiTFSI-based electrolytes, though the ionic conductivity of Hückel anion-based electrolytes are lower,[11,18] prior studies have shown that their Li$^+$ transference numbers are significantly higher,[5,19] which helps to reduce concentration polarization during cycling, thereby enhancing cell stability. The ionic conductivity results are closely related to the ionic association properties, which will be shown by local structure speciation in the following section.

Local structure speciation

Raman spectroscopy provides insights into local ion association trends that influence Li$^+$ solvation, revealing the extent of ion pairing and solvent coordination, as a function of lithium salt concentration.

Li$^+$–anion interactions. Raman spectra (Fig. 3 and Fig. S1) detect the evolution and shift of the anion-related vibrational bands: the nitrile (C≡N) group stretching vibrations, $\nu_{C≡N}$, at ~2200–2250 cm^{-1}, and the C═N imidazole ring stretching vibrations, $\nu_{C═N_{ring}}$, ~1280–1340 cm^{-1}, with increasing salt concentration due to their sensitivity to the local Li$^+$–anion coordination environment.[41] They also appear separately from the signals of the solvent, compared to other Raman peaks of the anions (e.g., δ_{NCN} bending vibration, Fig. S1b), and thus are more reliable for peak fitting analyses for estimating the concentration-dependent speciation.

We observed a similar behavior of the $\nu_{C≡N}$ vibrations of TDI, PDI, and HDI anions in DOL:DME that is also comparable to those in previous works with other oligoethers.[42,43] Particularly, the vibration arises from a strong and asymmetric band centered at ~2224 cm^{-1}, and a weak shoulder at ~2240 cm^{-1} with intensities corresponding to concentration variations from 0.1 to 2.0 M. The presence of a weak shoulder signals that there is a small fraction of polyanionic aggregates (e.g. dimer or chain type)[42] that exist even at the lowest concentration. Similar results between the three anions suggest that the length of the perfluoroalkyl chain does not affect the coordination.

On the other hand, $\nu_{C═N_{ring}}$ (approximately 1280–1340 cm^{-1}) shows different band shapes in 0.6–2.0 M LiTDI electrolytes. It splits into two peaks at 1305 and 1313 cm^{-1}–previously assigned to free imidazole nitrogen and Li-coordinated imidazole nitrogen, respectively.[42] Another peak at 1278 cm^{-1} arises from the CH$_2$ twisting vibration of DME. It is relatively sharp in salt-rich solutions compared to that of pure DME, indicating conformational changes due to coordination with Li$^+$. Although these three bands strongly overlap in the spectra of LiPDI electrolytes, they are slightly resolved in those of LiHDI electrolytes, albeit not as distinctly as in LiTDI electrolytes, especially at the highest salt concentration. These differences in ring vibrations suggest that the length of the perfluoroalkyl chain could cause steric effects on the local structures of Li–N$_{ring}$ coordination.

Ionic speciation. To estimate the percentage of free and associated ionic species, we performed curve-fitting analyses on the nitrile vibrations following previous works.[19] The bands were fitted with three combined 60%-Gaussian and 40%-Lorentzian components (Fig. S2–S4) that described three different types of associates: the solvent-separated ion pairs (SSIPs), or free anions,[42] at ~2220 cm^{-1}, contact ion pairs (CIPs) at ~2230 cm^{-1}, and aggregates (AGGs) such as dimer, trimer, and chain, etc. at ~2240 cm^{-1}. The fractional profiles of these components (Fig. 3(d)–(f)), in general, show that CIPs are the dominant species in the 2.0 M electrolytes of three salts, and the fraction of AGGs scales with the salt concentration. Particularly in LiTDI electrolytes, the dominant SSIPs systematically drop by 29%, accompanied by a 22% and ~6% increase of CIPs and AGGs, respectively, by moving from the 0.1 to the 2.0 M electrolytes. A similar trend is observed for LiPDI, except that LiPDI forms about twice the amount of AGGs than LiTDI at the most concentrated electrolytes. In LiHDI electrolytes, CIPs account for ~60% of the total solvates, predominating over SSIPs and AGGs at all concentrations. Notably, the fraction of AGGs in 2.0 M LiHDI is the highest among the other counterparts.

Ion–solvent interactions. Shifts in the vibrational bands associated with DOL and DME, e.g., C–O and C–C stretching modes,[44–47] provide insights on concentration-dependence and the role of the perfluoroalkyl chain length of the anions on Li$^+$–solvent coordination (Fig. 4).

The vibrational mode of pure DOL at ~940 cm^{-1} (C–O stretching mode,[48] Fig. 4(a) and Fig. S1b) decreases in intensity but remains stable in position, with no new bands emerging,

This journal is © the Owner Societies 2025

Phys. Chem. Chem. Phys., 2025, **27**, 18778–18788 | **18781**
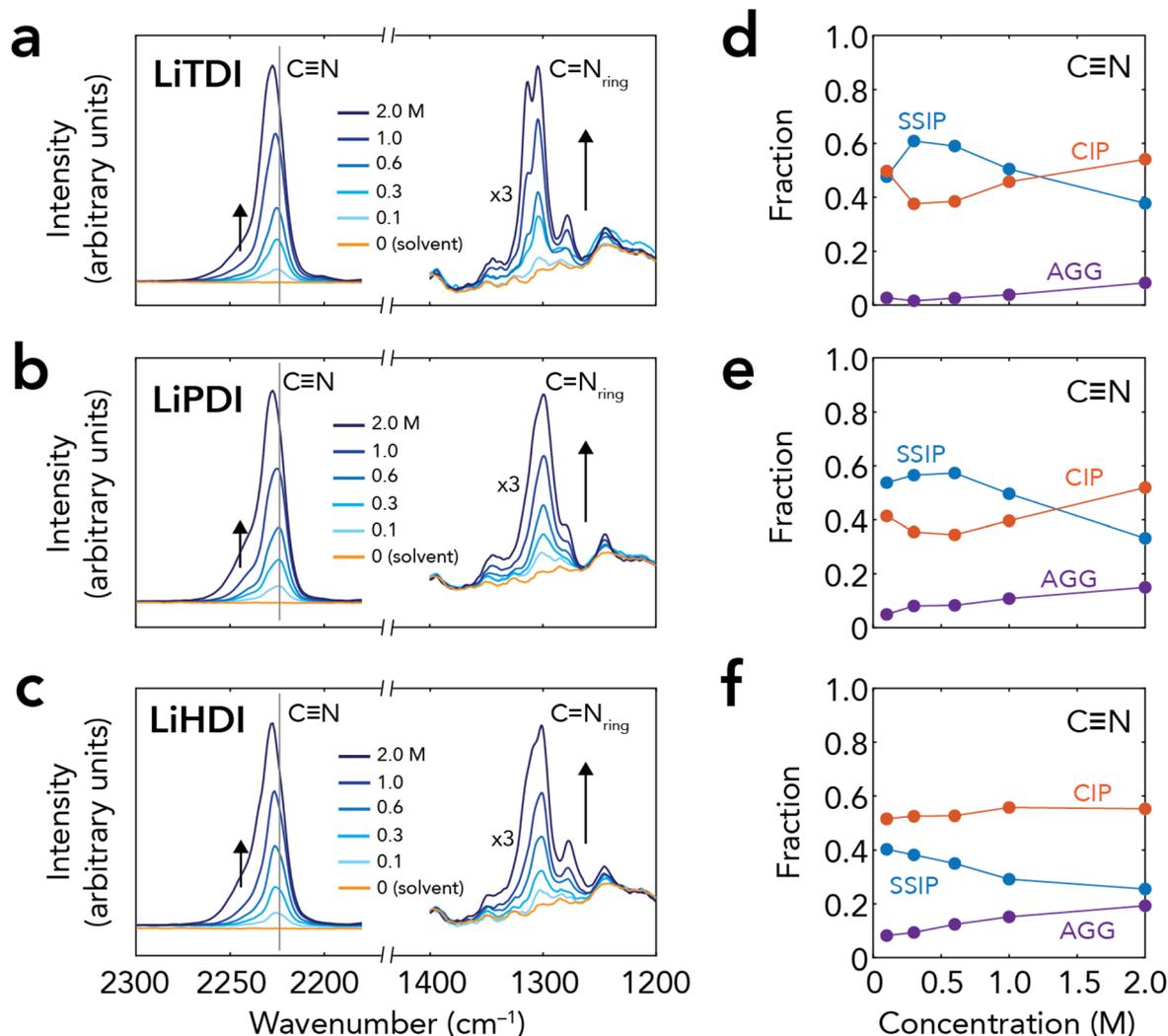
Fig. 3 Concentration-dependent ion–ion interactions revealed by Raman spectra of (a) LiTDI, (b) LiPDI and (c) LiHDI in the solvent mixture of DOL: DME (1 : 1, v/v) showing the evolution and shifts of bands corresponding to the nitrile stretches ($\sim$2225 cm^{-1}) and the C=N stretches of the imidazole ring ($\sim$1300 cm^{-1}). (d)–(f) Deconvolution of the nitrile stretching region (cf. Fig. S1) provides speciation of CIP and AGG.

even as the salt concentration increases up to 2.0 M. This indicates that DOL molecules do not significantly participate in the solvation structure of Li$^+$ cations, even at the (near) saturation of 2.0 M salt (3.6 DOL per Li), which aligns with the same observation with LiTFSI-based electrolytes in the same solvent system.[47] In the latter system, Li$^+$–DOL interaction becomes important to fulfil the Li$^+$ coordination shell in the ultra-high concentration region,[47] which could not be achieved in our case due to solubility limitations.

On the other hand, the bands of neat DME (850 and 823 cm^{-1}, the coupled C–O stretching ($\nu_{(CO)}$) and CH$_2$ rocking ($\delta_{(CH_2)}$) vibrations,[49] Fig. 4(b) and Fig. S1c) in our electrolytes decrease in intensity while there is an emerging band at 874 cm^{-1} – the value of bound DME,[44–47]–upon increasing the salt concentration up to 2.0 M. These results suggest that DME molecules preferentially coordinate Li$^+$ cations. We explain the less active role of DOL in our case by (1) the sufficient amounts of DME (e.g., 2.2 molecules per Li in

2.0 M of salt) to coordinate Li$^+$, and (2) the preferential bidentate configuration between Li$^+$–DME dominating the less favourable monodentate Li$^+$–DOL.[13,46] Furthermore, the numbers of coordinated solvent molecules, derived from the $\nu_{(CO)}$ + $\delta_{(CH_2)}$ band intensities of bound and free DME using eqn (1), decreases from 4.2–5.0 in 0.1 M salt to 1.5–2.0 in 2.0 M salt (Table S2). This suggests that, as the salt concentration increases, the local Li$^+$–solvent interactions in the primary solvation shell are increasingly replaced by Li$^+$–anion interactions, consistent with the higher amounts of CIPs and AGGs mentioned earlier. Nonetheless, the global population of Li-bound DME is still increasingly important at higher salt concentrations, given by the main appearance of the bound DME band at 874 cm^{-1} (Fig. 4(b) and (c)). Additionally, its broadening in the spectra of 0.6–2.0 M LiHDI electrolytes than those of LiTDI and LiPDI electrolytes (Fig. 4(c)) could be attributed to the geometric effect of the longer perfluoroalkyl chain of HDI anion on F···Li$^+$–DME coordination in the dimer- or chain-type AGG structures.

18782 | Phys. Chem. Chem. Phys., 2025, 27, 18778–18788

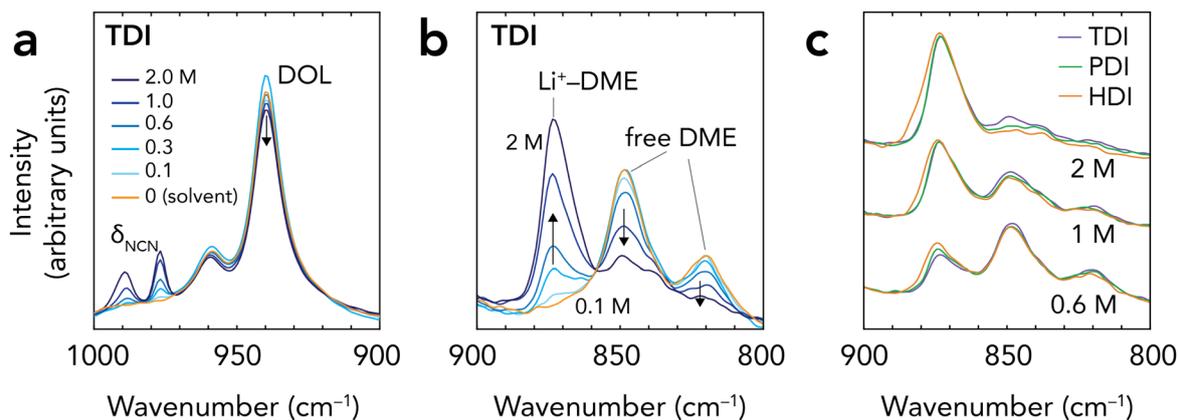This journal is © the Owner Societies 2025

Fig. 4 Ion–solvent interactions revealed through Raman spectra of the (a) C–O stretching vibrations of DOL and (b) the combined C–O stretching (ν_{CO}) and CH$_2$ rocking (δ_{CH_2}) vibrations of DME in 0.1–2.0 M LiTDI electrolytes. Raman spectra of LiPDI and LiHDI-electrolytes showing the same regions are provided in Fig. S1. (b) Comparison of the $\nu_{CO} + \delta_{CH_2}$ vibrations of DME in 2.0 M LiTDI, LiPDI, and LiHDI suggesting stronger coordination of DME with Li$^+$ cation in LiHDI-based electrolytes.

MD simulations

To complement the experimental findings, MD simulations offer an atomistic perspective, elucidating the coordination environment of Li$^+$ across different concentrations.

Fig. 5(a) reveal a consistent trend of Li$^+$ interactions with various atoms across all three systems: TDI, PDI, and HDI. In general, lithium ions primarily coordinate with the nitrogen atoms of the ring (N$_{ring}$) and the nitrile groups (N$_{C\equiv N}$) of the anion, and the oxygen atoms from the DME molecules. In particular, the RDFs indicate minimal interaction between

lithium and the oxygen atoms from DOL, suggesting that DOL does not participate in the first coordination shell of Li$^+$.

The sharp peaks in the RDFs at short distances confirm strong coordination between Li$^+$ and the nitrogen atoms from the anion and the oxygen atoms from DME, with the coordination environment being similar across TDI, PDI, and HDI. This trend shows that regardless of the size of the anion, the primary solvation shell of lithium is dominated by interactions with the nitrogen atoms of the anions and oxygen atoms of the DME solvent.
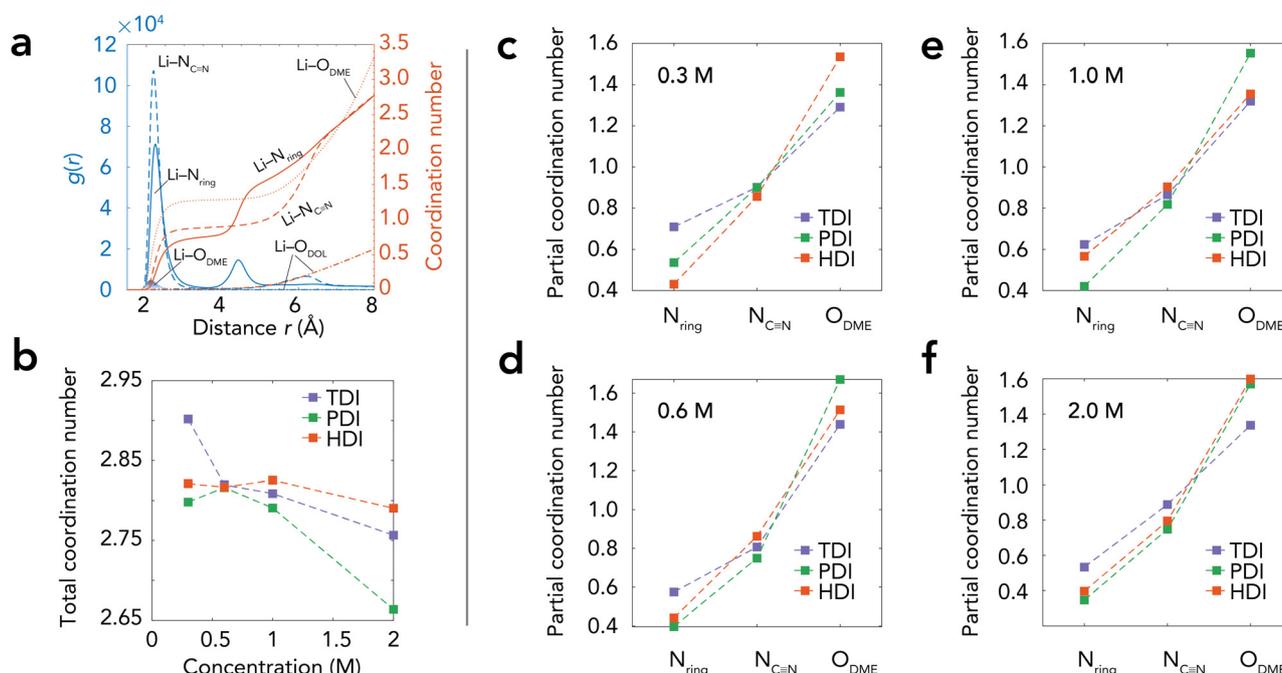

Fig. 5 MD simulation results. (a) Radial distribution functions $g(r)$ (left) dependence on the distance to a lithium ion for nitrogen atoms (nitrile- and $\nu_{CN_{ring}}$-types) and oxygen atoms of DME and DOL. Their integrated curves (right) show total coordination numbers. (b) Total coordination numbers of Li$^+$ for the three electrolyte systems across 0.3–2 M. (c)–(f) Partial coordination numbers of Li$^+$ with nitrogen atoms of the $\nu_{CN_{ring}}$ and nitrile group (N$_{C\equiv N}$), and oxygen atoms from DME (O$_{DME}$) at each concentration.

This journal is © the Owner Societies 2025

Phys. Chem. Chem. Phys., 2025, **27**, 18778–18788 | **18783**

The total CNs derived from the RDFs (Fig. 5(b)) remains fairly stable across concentrations. The general trend shows a decrease in CN with increasing salt concentration for PDI and TDI, especially at 2.0 M.

The partial CNs (pCNs) of Li⁺ (Fig. 5(c)–(f)), offer further insight into the coordination environment. Across all concentrations and anion types, the coordination of Li⁺ with oxygen atoms of DME consistently exhibits the highest pCNs, confirming the dominant role of DME in the lithium coordination shell. In contrast, the coordination with N_{ring} and $N_{C\equiv N}$ remains relatively low, reflecting their secondary role in the coordination structure. At 0.3 M, the coordination with O_{DME} increases as the size of the anion increases, indicating that steric restrictions from larger anions, such as PDI and HDI, limit their ability to coordinate directly with Li⁺. This spatial hindrance allows DME to occupy a more prominent role in the coordination shell. In contrast, the smallest anion (TDI) exhibits higher pCNs with Li⁺ for both $\nu_{CN_{ring}}$ and $N_{C\equiv N}$, as its smaller size allows closer access to Li⁺. As the concentration increases, subtle trends emerge. At intermediate concentrations, particularly 0.6 M, there is a slight increase in nitrogen coordination for TDI, suggesting that the balance between anion size and concentration briefly enhances its coordination efficiency. This effect diminishes at higher concentrations. For larger anions (PDI and HDI), the coordination with O_{DME} becomes more pronounced at higher concentrations (1.0 M and 2.0 M). This highlights the competitive advantage of DME over nitrogen atoms in coordinating with Li⁺, especially in systems where steric effects restrict anion proximity.

This trend, even though it contradicts our above Raman spectra suggesting that Li⁺ increasingly interacts with anions at 1.0 and 2.0 M concentrations due to ion pairing (CIP, AGG, *cf.* Fig. 3), still agrees with the global increasing Li⁺-bound DME population derived from the Raman spectra at these concentrations (*cf.* Fig. 4(b) and (c)). This apparent inconsistency may arise from differences in experimental and simulation time-scales, steric effects of larger anions that could physically hinder Li⁺ from coordinating with other anions (thus favoring Li⁺–DME coordination), or limitations in force field parameterization in capturing long-range aggregation effects. In particular, non-polarizable force fields, such as OPLS-AA, assume that the electrostatic degrees of freedom of the molecules remain fixed and do not respond to changes in their environment.[50] This simplification often leads to an underestimation of ion pairing interactions compared to experimental data,[51] potentially explaining why MD simulations predict stronger Li⁺–DME coordination than Raman spectroscopy suggests. Additional experimental and computational studies, such as nuclear magnetic resonance spectroscopy or *ab initio* MD, may help resolve this discrepancy.

Overall, the coordination environment reflects a dynamic balance between anion size and electrolyte concentration. While nitrogen atoms play a minor role in the solvation structure, DME consistently dominates due to its sterically unhindered access to Li⁺ ions. These findings reinforce the conclusion that DME acts as the primary coordinating solvent,

while nitrogen coordination is modulated by both anion size and ion density.

Modeling LiPS solubility

Lower LiPS solubility is critical for enhancing the performance and cycle life of Li–S batteries. To predict the solubility of Li_2S_8 in LiTDI, LiPDI, and LiHDI-based electrolytes, we employed a COSMO-RS approach in combination with a supervised machine learning model, following a methodology similar to our previous work.[21]

$$\log_{10}(s_{predicted}) = 7.84 \cdot \mu(-0.02) - 109.25 \cdot \mu(0.01) + 10.17 \quad (2)$$

The chemical potentials $\mu(\sigma)$ were computed using COSMOtherm and incorporated into a quantitative structure–property relationship model to estimate Li_2S_8 solubility. These potentials were derived from local molecular environments identified *via* spectroscopic speciation, with mole fractions (Table S3) incorporated accordingly. A range of surface charge density values (σ = ±0.03, ±0.02, ±0.01, and 0.0 eÅ⁻²) were used to construct the chemical potential profiles (Fig. S5). The multiple linear regression model in eqn (2) was recalibrated using updated COSMOtherm software and validated against experimental solubility data.[21]

As shown in Table 1, Li_2S_8 solubility decreases significantly—by nearly a factor of five—as the salt concentration increases from 1.0 M to 2.0 M. At 1.0 M, LiTDI shows the highest predicted solubility, followed by LiPDI and LiHDI. However, at 2.0 M, all three electrolytes exhibit markedly lower solubility, with LiPDI and LiHDI slightly outperforming LiTDI. This trend is likely driven by the higher viscosity and longer perfluoroalkyl chains of LiPDI and LiHDI, which promote stronger ion association and hinder LiPS transport.

Our previous COSMO-RS simulations[21] predicted that Li_2S_8 exhibits a lower chemical potential—and thus lower solubility—in LiTDI-based electrolytes as compared to LiTFSI-based ones. This prediction is supported by NMR diffusion studies, which showed the hydrodynamic radius of Li⁺ in LiTDI-based electrolytes to increase by approximately 20% upon the addition of Li_2S_8, indicating stronger complexation.[11] In contrast, no significant change was observed for LiTFSI-based electrolytes under similar conditions. Furthermore, *ab initio* molecular dynamics simulations by Chen *et al.*[11] revealed that LiTDI-based electrolytes favor formation of Li_2S_4 dimers, whereas LiTFSI-based electrolytes tend to form a broader distribution of PS species, such as Li_2S_3 and Li_2S_5. These differences are attributed to variations in Li⁺ solvation and anion coordination environments. The reactive imide and nitrile functional groups

Table 1 Predicted Li_2S_8 solubility ($s_{predicted}$, M) of LiTDI, LiPDI and LiHDI in DOL:DME

	1.0 M salt	2.0 M salt
LiTDI	0.229	0.034
LiPDI	0.160	0.026
LiHDI	0.157	0.026

18784 | *Phys. Chem. Chem. Phys.*, 2025, **27**, 18778–18788

This journal is © the Owner Societies 2025

on the Hückel anions may also stabilize sulfur species through selective binding, as previously shown for nitrile functionalized salts.[52] To gain deeper insight into LiPS dynamics during battery operation, we complemented our modeling with *operando* Raman spectroscopy.

Operando Raman spectroscopy

Operando Raman spectroscopy provides semiquantitative insights into the effects of concentration on LiPS chain length evolution, solubility, and diffusion in the electrolytes studied. During the first discharge plateau (2.4 V), Raman spectra of Li–S cells using 1.0 and 2.0 M LiTDI (Fig. 6(a), (b) and Fig. S6) show similar growth of salient Raman peaks corresponding to various LiPS species, consistent with previous studies in the same solvent system.[22–24] These include the 369 cm^{-1} peak for S_8^{2-}, the 400 and 451 cm^{-1} peaks for long-chain LiPSs (S_{6-8}^{2-}), and the 534 cm^{-1} peak for $S_3^{\bullet-}$ originated from S_6^{2-} disproportionation ($S_6^{2-} \rightleftharpoons 2S_3^{\bullet-}$). Although $S_3^{\bullet-}$ is not stabilized in DOL:DME solvent, its strong Raman signal arises from resonance coupling between the laser excitation wavelength (633 nm) with the molecular absorbance of the species at 617–627 nm.[53,54] Furthermore, the shift of the 451 cm^{-1} peak to 484 cm^{-1} on the 2.3–2.1 V slope suggests increasing S_4^{2-} concentration.[22–24] Similar LiPS evolution patterns were observed in 0.3 M LiTDI (Fig. S6), as well as in LiPDI (Fig. S7) and LiHDI (Fig. S8) at all concentrations, suggesting that the evolution of the LiPS chain length is independent of salt concentration.

The time-dependent LiPS growth curves reveal how salt concentration influences LiPS dissolution and diffusion (Fig. 6(c)–(e) and Fig. S9). Analyses focus on the first discharge plateau, where highly soluble and reactive long-chain LiPS (S_{6-8}^{2-}) dominate the electrochemistry and drive the shuttle effect. The LiPS growth curves directly correlate with the first discharge plateau length, with higher salt concentrations (0.3 → 2.0 M) improving capacity and, in turn, delaying the LiPS growth. The delay is ∼ 50–60 min in 2.0 M LiTDI (Fig. 6(c)) and 2.0 M LiPDI (Fig. 6(d)), but extends to 120 min in 2.0 M LiHDI (Fig. 6(e)), suggesting slower long-chain LiPS conversion and possible reducing LiPS shuttle. Notably, high LiHDI concentrations introduce an extra plateau (2.17–2.09 V) and broader LiPS population profiles, likely due to slower long-chain LiPSs conversion,[55] and this also suggests reducing LiPS shuttle effect. These results collectively indicate that higher salt concentrations slow LiPS diffusion toward the Li anode while enhancing LiPS redox conversion efficiency.

Furthermore, a higher salt concentration reduces the solubility and/or diffusion of LiPS, as evidenced by the downward trend in the maximum LiPS population across all electrolytes. This aligns with the above COSMO-RS predictions of more than 80% decrease in LiPS solubility when increasing salt concentration from 1.0 to 2.0 M. Among 1.0 and 2.0 M electrolytes,
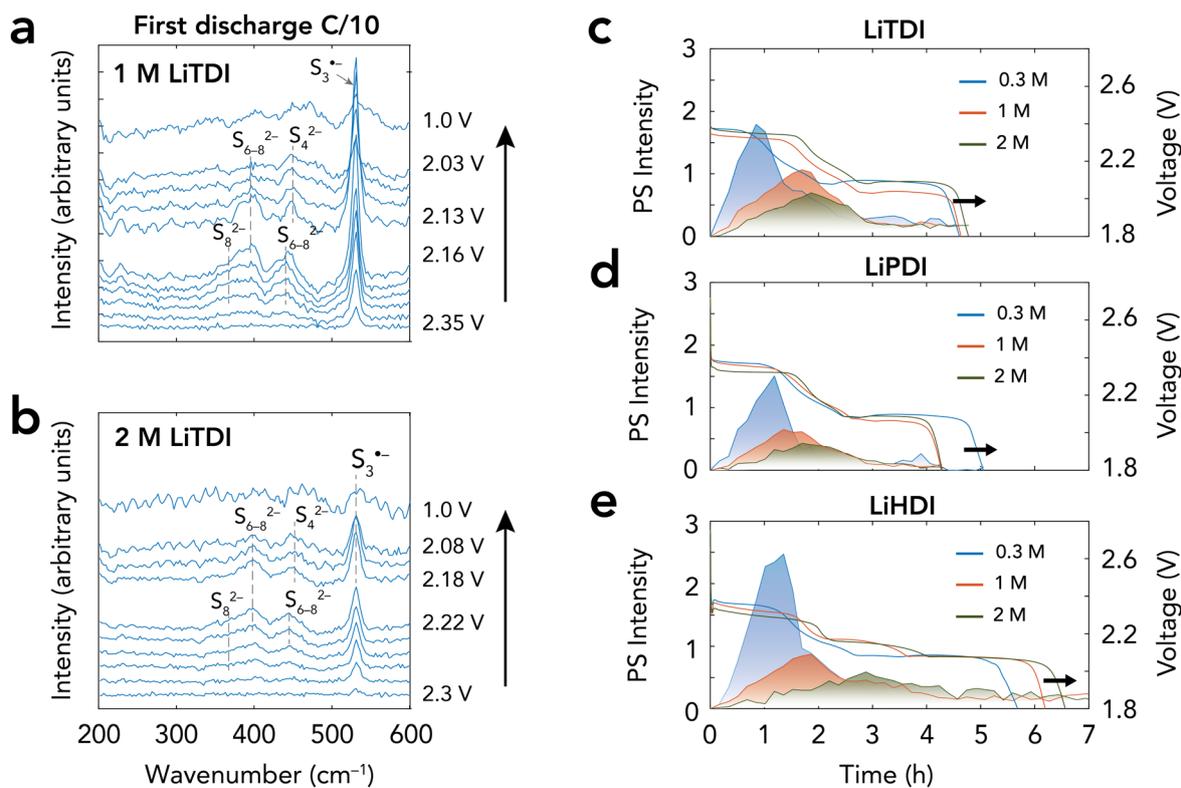

Fig. 6 *Operando* Raman experiments reveal that salt concentration regulates LiPS solubility and diffusion. (a), (b) Raman spectra sequence during discharge (C/10-rate) for 1.0 and 2.0 M LiTDI cells. (c)–(e) Comparison of average LiPS Raman intensities (lines with shades) and voltage profiles (solid lines) in cells with 0.3, 1.0, and 2.0 M electrolytes: (c) LiTDI, (d) LiPDI, and (e) LiHDI.

This journal is © the Owner Societies 2025

Phys. Chem. Chem. Phys., 2025, **27**, 18778–18788 | **18785**

LiPDI and LiHDI exhibit lower LiPS populations than LiTDI, supporting predictions that longer perfluoroalkyl chains reduce LiPS solubility. However, the inverse trend between LiPDI and LiHDI suggests slower long-chain LiPS conversion allows greater LiPS accumulation at the anode. The highest detected LiPS levels in 0.3 M LiHDI electrolyte may be explained by small Li/DME ratio but high degree of Li-anion interactions, leaving more free solvent (DME) available for LiPS dissolution.

Electrochemical performance in Li–S batteries

Finally, to evaluate the practical implications of the Hückel-type anion design on Li–S battery performance, we investigated the galvanostatic cycling behavior of cells employing 2.0 M LiTDI, LiPDI, and LiHDI electrolytes at a C/10 rate (Fig. 7). We limited our battery tests to only 2.0 M because (1) our previous study showed better performance on LiTDI,[18] and (2) spectroscopic evidence and COSMO-RS modeling provide low free solvent population (*cf.* Fig. 4) and less LiPS solubility (*cf.* Fig. 6(c)–(e)).

The voltage profiles over 100 cycles (Fig. 7(a)–(c)) reveal the characteristic two-plateau discharge behavior of sulfur cathodes for all three 2.0 M electrolytes, indicative of effective sulfur redox chemistry. LiHDI exhibited the highest initial capacity (800 mAh g^{-1}), while LiTDI and LiPDI showed slightly lower initial capacities. Notably, the LiHDI-based cell displayed excellent retention of charge profile shape over extended cycling, suggesting enhanced electrochemical stability.

The long-term cycling performance is summarized in Fig. 7(d). All three electrolytes enable discharge capacities in the range of 400–500 mAh g^{-1}, while the overcharge capacities differentiate the CEs between them.

The LiHDI-based electrolyte exhibited the highest CE (85%). While this represents an improvement over the LiTDI- and LiPDI-based electrolytes, it still falls short. Preliminary tests with an addition of LiNO$_3$ to the LiHDI-based electrolyte demonstrate that the CE can be significantly enhanced, reaching close to 100% (Fig. S10). This improvement is likely due to the formation of a robust solid electrolyte interphase enriched with highly conductive LiN$_x$O$_y$ and Li$_3$N species, which can effectively suppress LiPS shuttling and stabilize the lithium metal surface.[56]

4 Conclusions

This study systematically links the structural and physicochemical properties of LiTDI, LiPDI, and LiHDI-based electrolytes to their effects on LiPS solubility, diffusion, and electrochemical performance in Li–S batteries. *Ex situ* Raman spectroscopy and MD simulations confirm that Li$^+$ preferentially coordinates with DME, while increasing salt concentration enhances ion pairing that controls electrolyte transport properties. Among the studied electrolytes, LiHDI exhibited the highest amount of aggregates at 2.0 M, highlighting the role of perfluoroalkyl chain length in ion association.
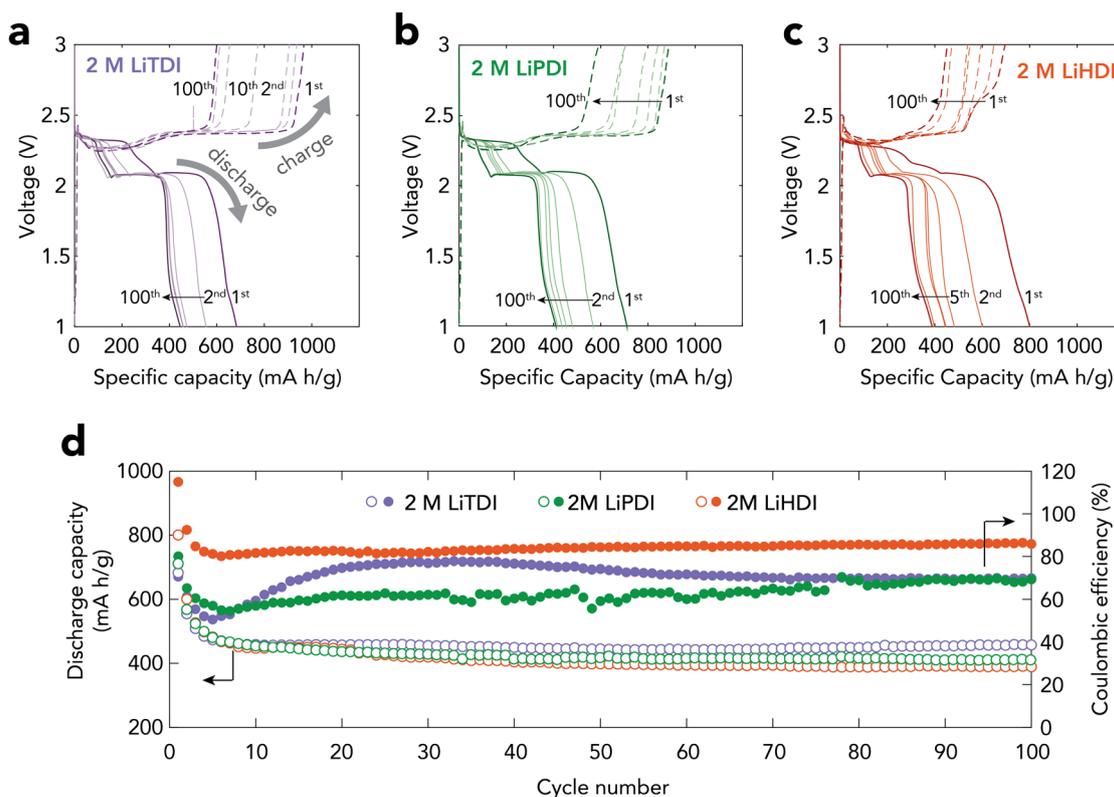

Fig. 7 (a)–(c) Galvanostatic charge–discharge profiles of Li–S cells cycled at C/10 for 100 cycles using electrolytes containing 2.0 M of (a) LiTDI, (b) LiPDI, and (c) LiHDI, respectively. (d) Corresponding discharge capacities and CEs of the Li–S cells over 100 cycles.

18786 | *Phys. Chem. Chem. Phys.*, 2025, **27**, 18778–18788

This journal is © the Owner Societies 2025

COSMO-RS modeling predicts a significant decrease in LiPS solubility with rising salt concentration with LiPDI and LiHDI showed slightly slower LiPS diffusion. *Operando* Raman spectroscopy further supports that higher salt concentrations decrease the dissolution and diffusion of long-chain LiPS, contributing to improved battery stability. Although the salts maintained stable discharge capacities, incorporating appropriate additives may improve the CE. These findings suggest that Hückel anion-based electrolytes, with tailored salt ratios, hold significant promise for advancing future Li–S battery technologies.

Author contributions

Aginmariya Kottarathil: writing – review & editing, writing – original draft, methodology, investigation, formal analysis, data curation, conceptualization of all parts of the work. N Tan Luong: writing – review & editing, visualization, methodology, investigation, formal analysis, data curation, conceptualization and validation of Raman & *operando* Raman experiments. Carolina Cruz Cardona: investigation, formal analysis, data curation, writing – original draft of MD simulation part. Steffen Jeschke: review & editing, validation of COSMO-RS modeling. Tomooki Hosaka: review & editing, conceptualization. Grazyna Zofia Zukowska: methodology, review & editing. Maciej Marczewski: conceptualization, editing. Wladyslaw Wieczorek and Patrik Johansson: writing – review & editing, supervision, resources, project administration, methodology, funding acquisition conceptualization.

Conflicts of interest

There are no conflicts to declare.

Data availability

The data supporting this article have been included as part of the SI. The raw data is available upon request from the authors.

Supplementary information available: The supplementary information includes additional experimental and computational details, supplementary Raman spectra with peak fitting, raw data from *operando* Raman experiments, and additional electrochemical results. Tables summarizing the Raman and molecular dynamics simulation results are also provided. See DOI: **https://doi.org/10.1039/d5cp02052b**

Acknowledgements

References

1 K. Xu, *Chem. Rev.*, 2004, **104**, 4303–4418.
2 Y.-K. Liu, C.-Z. Zhao, J. Du, X.-Q. Zhang, A.-B. Chen and Q. Zhang, *Small*, 2023, **19**, 2205315.
3 S. Paillet, G. Schmidt, S. Ladouceur, J. Fréchette, F. Barray, D. Clément, P. Hovington, A. Guerfi, A. Vijh and I. Cayrefourcq, *et al.*, *J. Power Sources*, 2015, **294**, 507–515.
4 A. Bitner-Michalska, G. M. Nolis, G. Żukowska, A. Zalewska, M. Poterała, T. Trzeciak, M. Dranka, M. Kalita, P. Jankowski and L. Niedzicki, *et al.*, *Sci. Rep.*, 2017, **7**, 40036.
5 M. Armand, P. Johansson, M. Bukowska, P. Szczeciński, L. Niedzicki, M. Marcinek, M. Dranka, J. Zachara, G. Żukowska and M. Marczewski, *et al.*, *J. Electrochem. Soc.*, 2020, **167**, 070562.
6 A. Manthiram, Y. Fu, S.-H. Chung, C. Zu and Y.-S. Su, *Chem. Rev.*, 2014, **114**, 11751–11787.
7 M. Zhao, B.-Q. Li, X.-Q. Zhang, J.-Q. Huang and Q. Zhang, *ACS Cent. Sci.*, 2020, **6**, 1095–1104.
8 L.-P. Hou, Y. Li, Z. Li, Q.-K. Zhang, B.-Q. Li, C.-X. Bi, Z.-X. Chen, L.-L. Su, J.-Q. Huang and R. Wen, *et al.*, *Angew. Chem., Int. Ed.*, 2023, **62**, e202305466.
9 A. Manthiram, Y. Fu and Y.-S. Su, *Acc. Chem. Res.*, 2013, **46**, 1125–1134.
10 H. Raza, S. Bai, J. Cheng, S. Majumder, H. Zhu, Q. Liu, G. Zheng, X. Li and G. Chen, *Electrochem. Energy Rev.*, 2023, **6**, 29.
11 J. Chen, K. S. Han, W. A. Henderson, K. C. Lau, M. Vijayakumar, T. Dzwiniel, H. Pan, L. A. Curtiss, J. Xiao and K. T. Mueller, *et al.*, *Adv. Energy Mater.*, 2016, **6**, 1600160.
12 L. Suo, Y.-S. Hu, H. Li, M. Armand and L. Chen, *Nat. Commun.*, 2013, **4**, 1481.
13 K. S. Han, J. Chen, R. Cao, N. N. Rajput, V. Murugesan, L. Shi, H. Pan, J.-G. Zhang, J. Liu and K. A. Persson, *et al.*, *Chem. Mater.*, 2017, **29**, 9023.
14 B. D. Adams, E. V. Carino, J. G. Connell, K. S. Han, R. Cao, J. Chen, J. Zheng, Q. Li, K. T. Mueller and W. A. Henderson, *et al.*, *Nano Energy*, 2017, **40**, 607–617.
15 J. Scheers, S. Fantini and P. Johansson, *J. Power Sources*, 2014, **255**, 204.
16 G. Liu, Q. Sun, Q. Li, J. Zhang and J. Ming, *Energy Fuels*, 2021, **35**, 10405–10427.
17 L. Niedzicki, G. Zukowska, M. Bukowska, P. Szczeciński, S. Grugeon, S. Laruelle, M. Armand, S. Panero, B. Scrosati and M. Marcinek, *Electrochim. Acta*, 2010, **55**, 1450.
18 A. Kottarathil, Z. Slim, H. A. Ishfaq, S. Jeschke, G. Z. Żukowska, M. Marczewski, K. Lech, P. Johansson and W. Wieczorek, *J. Electrochem. Soc.*, 2024, **171**, 070506.
19 A. Szczesna-Chrzan, M. Vogler, P. Yan, G. Z. Żukowska, C. Wölke, A. Ostrowska, S. Szymańska, M. Marcinek,

This journal is © the Owner Societies 2025

Phys. Chem. Chem. Phys., 2025, **27**, 18778–18788 | **18787**

M. Winter and I. Cekic-Laskovic, et al., J. Mater. Chem. A, 2023, **11**, 13483–13492.

20 F. Lindgren, C. Xu, L. Niedzicki, M. Marcinek, T. Gustafsson, F. F. Björefors, K. Edstrom and R. Younesi, ACS Appl. Mater. Interfaces, 2016, **8**, 15758–15766.

21 S. Jeschke and P. Johansson, Batteries Supercaps, 2021, **4**, 1156–1162.

22 R. Bouchal, A. Boulaoued and P. Johansson, Batteries Supercaps, 2020, **3**, 397–401.

23 M. Hagen, P. Schiffels, M. Hammer, S. Dörfler, J. Tübke, M. Hoffmann, H. Althues and S. Kaskel, J. Electrochem. Soc., 2013, **160**, A1205.

24 J. Hannauer, J. Scheers, J. Fullenwarth, B. Fraisse, L. Stievano and P. Johansson, ChemPhysChem, 2015, **16**, 2755–2759.

25 K. Balasubrahmanyam and G. J. Janz, J. Am. Chem. Soc., 1970, **92**, 4189–4193.

26 D. M. Seo, O. Borodin, S.-D. Han, Q. Ly, P. D. Boyle and W. A. Henderson, J. Electrochem. Soc., 2012, **159**, A553.

27 S. Plimpton, J. Comput. Phys., 1995, **117**, 1–19.

28 W. L. Jorgensen, D. S. Maxwell and J. Tirado-Rives, J. Am. Chem. Soc., 1996, **118**, 11225–11236.

29 W. L. Jorgensen and J. Tirado-Rives, Proc. Natl. Acad. Sci. U. S. A., 2005, **102**, 6665–6670.

30 L. S. Dodda, J. Z. Vilseck, J. Tirado-Rives and W. L. Jorgensen, J. Phys. Chem. B, 2017, **121**, 3864–3870.

31 L. S. Dodda, I. Cabeza de Vaca, J. Tirado-Rives and W. L. Jorgensen, Nucleic Acids Res., 2017, **45**, W331–W336.

32 J. Self, K. D. Fong and K. A. Persson, ACS Energy Lett., 2019, **4**, 2843–2849.

33 Z. Yu, P. E. Rudnicki, Z. Zhang, Z. Huang, H. Celik, S. T. Oyakhire, Y. Chen, X. Kong, S. C. Kim and X. Xiao, et al., Nat. Energy, 2022, **7**, 94–106.

34 A. Klamt, V. Jonas, T. Bürger and J. C. Lohrenz, J. Phys. Chem. A, 1998, **102**, 5074.

35 A. Klamt, Wiley Interdiscip. Rev.: Comput. Mol. Sci., 2011, **1**, 699.

36 COSMOtherm C3.0, release 15.01. Leverkusen, Germany: COS-MOlogicGmbH Co. KG; 2014. https://www.cosmologic.de.

37 TURBOMOLE V7.2 2017, a development of University of Karlsruhe and Forschungszentrum Karlsruhe GmbH, 1989-2007, TURBOMOLE GmbH, since 2007; available from https://www.turbomole.com.

38 J. P. Perdew, Phys. Rev. B: Condens. Matter Mater. Phys., 1986, **33**, 8822.

39 A. D. Becke, Phys. Rev. A: At., Mol., Opt. Phys., 1988, **38**, 3098.

40 M. Broszkiewicz, A. Zalewska and L. Niedzicki, Ionics, 2019, **25**, 3651–3660.

41 J. Scheers, L. Niedzicki, G. Z. Żukowska, P. Johansson, W. Wieczorek and P. Jacobsson, Phys. Chem. Chem. Phys., 2011, **13**, 11136–11147.

42 P. Jankowski, M. Dranka, G. Z. Zukowska and J. Zachara, J. Phys. Chem. C, 2015, **119**, 9108–9116.

43 P. Jankowski, M. Dranka and G. Z. Żukowska, J. Phys. Chem. C, 2015, **119**, 10247–10254.

44 D. Brouillette, D. E. Irish, N. J. Taylor, G. Perron, M. Odziemkowski and J. E. Desnoyers, Phys. Chem. Chem. Phys., 2002, **4**, 6063–6071.

45 K. Ueno, R. Tatara, S. Tsuzuki, S. Saito, H. Doi, K. Yoshida, T. Mandai, M. Matsugami, Y. Umebayashi and K. Dokko, et al., Phys. Chem. Chem. Phys., 2015, **17**, 8248–8257.

46 J. Zhou, W. Gong, X. Meng, J. Zhang, X. Zhou, S. Chen, C. W. Bielawski and J. Geng, Appl. Phys. Rev., 2023, **10**, 041401.

47 A. Hockmann, F. Ackermann, D. Diddens, I. Cekic-Laskovic and M. Schönhoff, Faraday Discuss., 2024, **253**, 343–364.

48 V. Mohaček-Grošev, K. Furić and H. Ivanković, Vib. Spectrosc., 2013, **64**, 101–107.

49 H. Yoshida and H. Matsuura, J. Phys. Chem. A, 1998, **102**, 2691–2699.

50 M. Jorge, J. Chem. Phys., 2024, **161**, 180901.

51 I. Leontyev and A. Stuchebrukhov, Phys. Chem. Chem. Phys., 2011, **13**, 2613–2626.

52 J. Song, T. Xu, M. L. Gordin, P. Zhu, D. Lv, Y.-B. Jiang, Y. Chen, Y. Duan and D. Wang, Adv. Funct. Mater., 2014, **24**, 1243–1250.

53 K. H. Wujcik, D. R. Wang, A. Raghunathan, M. Drake, T. A. Pascal, D. Prendergast and N. P. Balsara, J. Phys. Chem. C, 2016, **120**, 18403–18410.

54 B. Zhang, Z. Wang, H. Ji, H. Zhang, L. Li, J. Hu, S. Li and J. Wu, Chem. Commun., 2023, **59**, 4237–4240.

55 H. Shin, M. Baek, A. Gupta, K. Char, A. Manthiram and J. W. Choi, Adv. Energy Mater., 2020, **10**, 2001456.

56 Q. Jin, K. Zhao, L. Wu, L. Li, L. Kong and X. Zhang, J. Energy Chem., 2023, **84**, 22–29.

18788 | Phys. Chem. Chem. Phys., 2025, **27**, 18778–18788

This journal is © the Owner Societies 2025